

Harnessing disordered quantum dynamics for machine learning

Keisuke Fujii^{1,2,*} and Kohei Nakajima^{1,3,4}

¹*The Hakubi Center for Advanced Research, Kyoto University,
Yoshida-Ushinomiya-cho, Sakyo-ku, Kyoto 606-8302, Japan*

²*Department of Physics, Graduate School of Science, Kyoto University,
Kitashirakawa Oiwake-cho, Sakyo-ku, Kyoto 606-8502, Japan*

³*Graduate School of Informatics, Kyoto University,
Yoshida Honmachi, Sakyo-ku, Kyoto 606-8501, Japan*

⁴*JST, PRESTO, 4-1-8 Honcho, Kawaguchi, Saitama 332-0012, Japan*

(Dated: August 18, 2018)

Quantum computer has an amazing potential of fast information processing. However, realisation of a digital quantum computer is still a challenging problem requiring highly accurate controls and key application strategies. Here we propose a novel platform, quantum reservoir computing, to solve these issues successfully by exploiting natural quantum dynamics, which is ubiquitous in laboratories nowadays, for machine learning. In this framework, nonlinear dynamics including classical chaos can be universally emulated in quantum systems. A number of numerical experiments show that quantum systems consisting of at most seven qubits possess computational capabilities comparable to conventional recurrent neural networks of 500 nodes. This discovery opens up a new paradigm for information processing with artificial intelligence powered by quantum physics.

I. INTRODUCTION

Quantum physics, which is the fundamental framework of physics, exhibits rich dynamics, sufficient to explain natural phenomena in microscopic worlds. As Feynman pointed out [1], the simulation of quantum systems on classical computers is extremely challenging because of the high complexity of these systems. Instead, they should be simulated by using a machine of which the operation is based on the laws of quantum physics.

Motivated by the recent rapid experimental progress in controlling complex quantum systems, non-conventional information processing utilising quantum physics has been explored in the field of quantum information science [2, 3]. For example, certain mathematical problems, such as integer factorisation, which are believed to be intractable on a classical computer, are known to be efficiently solvable by a sophisticatedly synthesized quantum algorithm [4]. Therefore, considerable experimental effort has been devoted to realising full-fledged universal quantum computers [5, 6]. On the other hand, quantum simulators are thought to be much easier to implement than a full-fledged universal quantum computer. In this regard, existing quantum simulators have already shed new light on the physics of complex many-body quantum systems [7–9], and a restricted class of quantum dynamics, known as adiabatic dynamics, has also been applied to combinatorial optimisation problems [10–13]. However, complex real-time quantum dynamics, which is one of the most difficult tasks for classical computers to simulate [14–16] and has great potential to perform nontrivial information processing, is now waiting to be harnessed as a resource for more general purpose information processing. Specifically, the recent rapid progress

in sensing and Internet technologies has resulted in an increasing demand for fast intelligent big data analysis with low energy consumption. This has motivated us to develop brain-inspired information processing devices of a non-von Neumann type, on which machine learning tasks are able to run natively [17].

Here we propose a novel framework to exploit the complexity of real-time quantum dynamics for nonlinear and temporal learning problems. These problems include a variety of real-world tasks such as time-dependent signal processing, speech recognition, natural language processing, sequential motor control of robots, and stock market predictions. Our approach is based on a machine learning technique inspired by the way the brain processes information, so-called *reservoir computing* [4, 12, 19]. In particular, this framework focuses on real-time computing with time-varying input that requires the use of memory, unlike feedforward neural networks or deep neural networks [21]. In this framework, the low-dimensional input is projected to a high-dimensional dynamical system, which is typically referred to as a *reservoir*, generating transient dynamics that facilitates the separation of input states [22]. If the dynamics of the reservoir involve both adequate memory and nonlinearity [2], emulating nonlinear dynamical systems only requires adding a linear and static readout from the high-dimensional state space of the reservoir.

A number of different implementations of reservoirs have been proposed, such as abstract dynamical systems for echo state networks (ESNs) [12] or models of neurons for liquid state machines [19]. The implementations are not limited to programs running on the PC but also include physical systems, such as the surface of water in a laminar state [24], analogue circuits and optoelectronic systems [5, 26–29], and neuromorphic chips [30]. Recently, it has been reported that the mechanical bodies of soft and compliant robots have also been successfully

* fujii.keisuke.2s@kyoto-u.ac.jp

used as a reservoir [9–11, 34]. In contrast to the refinements required by learning algorithms, such as in deep learning [35], the approach followed by reservoir computing, especially when applied to real systems, is to find an appropriate form of physics that exhibits rich dynamics, thereby allowing us to outsource a part of the computation. Nevertheless, no quantum physical system has been employed yet as a physical reservoir.

Here we formulate quantum reservoir computing (QRC) and show, through a number of numerical experiments, that quantum dynamics can be used as a powerful reservoir. Although there have been several prominent proposals on utilising quantum physics in the context of machine learning [36–40], they are based on sophisticatedly synthesised quantum circuits on a full-fledged universal quantum computer. Contrary to these software approaches, the approach followed by QRC is to exploit the complexity of natural quantum dynamics for information processing, as it is. This is a great advantage, because we can utilise existing quantum simulators or complex quantum systems as resources to boost information processing. Among existing works on quantum machine learning [36–40], our approach is the first attempt to exploit quantum systems for temporal machine learning tasks, which essentially require a memory effect to the system. As we will see below, our benchmark results show that quantum systems consisting of 5–7 qubits already exhibit a powerful performance comparable to the ESNs of 100–500 nodes.

II. QUANTUM RESERVOIR COMPUTING

Definition of quantum reservoir dynamics.— A quantum system consisting of N qubits can be described by a $2^N \times 2^N$ hermitian density matrix ρ . The dynamics of a closed system is defined by the Hamiltonian H , a $2^N \times 2^N$ hermitian matrix, and the state $\rho(t)$ at time t evolves after a time interval τ to $\rho(t + \tau) = e^{-iH\tau}\rho(t)e^{iH\tau}$. An observable of the system is defined by a $2^N \times 2^N$ hermitian matrix O and its average value $\langle O \rangle = \text{Tr}[O\rho(t)]$ is obtained from the system. It is convenient to represent the density matrix as a vector \mathbf{x} in a 4^N -dimensional operator space (see Supplementary Information 1 for details). Then any physical operation is written as a linear map for the state \mathbf{x} . The unitary time evolution is rewritten as

$$\mathbf{x}(t + \tau) = U_\tau \mathbf{x}(t), \quad (1)$$

in terms of a $4^N \times 4^N$ matrix U_τ subject to $U_\tau U_\tau^\dagger = I$ reflecting unitarity (see Supplementary Information 1 for the detailed construction).

In order to exploit quantum dynamics for information processing, we have to introduce an input and the signals of the quantum system (see Fig. 1A). Suppose $\{s_k\}_{k=1}^M$ is an input sequence, where s_k can be a binary $s_k \in \{0, 1\}$ for a Boolean task or a continuous variable $s_k \in [0, 1]$ for a dynamical task. A temporal learning task

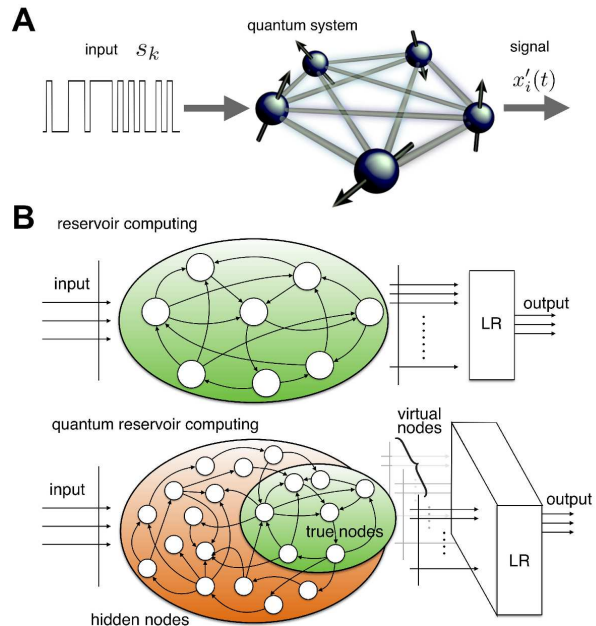


FIG. 1. **Information processing scheme in QRC.** (A) The input sequence $\{s_k\}$ is injected into the quantum system. The signal $x'_i(t)$ is obtained from each qubit. (B) Comparison between conventional (upper) and quantum (lower) reservoir computing approaches.

here is to find, using the quantum system, a nonlinear function $y_k = f(\{s_l\}_{l=1}^k)$ such that the mean square error between y_k and a target (teacher) output \bar{y}_k for a given task becomes minimum. To do so, at each time $t = k\tau$, the input signal s_k is injected into a qubit, say the 1st qubit, by replacing (or by using measurement and feedback) the 1st qubit with the state $\rho_{s_k} = |\psi_{s_k}\rangle\langle\psi_{s_k}|$, where

$$|\psi_{s_k}\rangle := \sqrt{1-s_k}|0\rangle + \sqrt{s_k}|1\rangle. \quad (2)$$

The signal is defined as an average value of a local observable on each qubit. We here employ, as observables, the Pauli operator Z_i acting on each i th qubit. Then the signal from the i th qubit at time t , denoted by $x'_i(t)$, is defined as follows:

$$x'_i(t) := \text{Tr}[(I + Z_i)/2\rho(t)]. \quad (3)$$

By appropriately choosing the basis in the operator space such that $x_i(t) = \text{Tr}[Z_i\rho(t)]$ ($i = 1, \dots, N$), the first N elements of the state $\mathbf{x}(t)$, which we refer to as the *true nodes*, are related to the signals $x'_i(t) = [1 + x_i(t)]/2$. Let us refer to the remaining $(4^N - N)$ nodes of $\mathbf{x}(t)$ as *hidden nodes*, as they are not employed as signals. The unique feature of QRC in the reservoir computing context is that the exponentially many hidden nodes are monitored from a polynomial number of signals from true nodes as shown in Fig. 1B. Here we do not consider the back action of the measurements to obtain the average values $\{x'_i(t)\}$ by considering an ensemble quantum system such as ensemble spin NMR systems [41, 42]. Otherwise we can simply

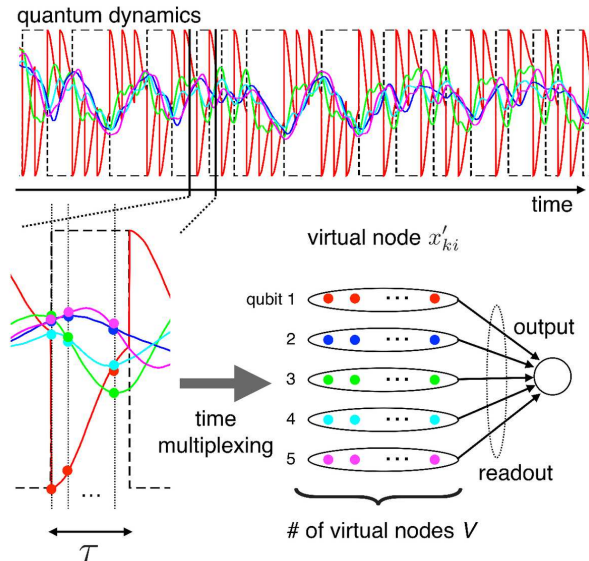


FIG. 2. **Quantum reservoir dynamics and virtual nodes.** The time interval τ is divided into V subdivided timesteps. At each subdivided timestep the signals are sampled. Using the NV signals as the virtual nodes for each timestep k in the learning phase, the linear readout weights $\{w_i^{\text{LR}}\}$ are trained for a task.

repeat the sampling to get the averaged values for other quantum systems.

Emerging nonlinearity from a linear system. — One might think that the quantum system is totally linear, and hence that we cannot employ it for learning tasks, which essentially require nonlinearity. However, this is not the case. Whereas dynamics is described as a linear map, information with respect to any kind of correlation among the true nodes exists in exponentially many degrees of freedom. Such correlation, or nonlinearity, is monitored through the true nodes via the linear dynamics U_τ among the true and hidden nodes. For example, in the hidden nodes, there exists a state corresponding to an observable $B_l = Z_i Z_j$, i.e. $x_l(t) = \text{Tr}[Z_i Z_j \rho(t)]$ storing correlation between $x_i(t) = \text{Tr}[Z_i \rho(t)]$ and $x_j(t) = \text{Tr}[Z_j \rho(t)]$, which can be monitored from another true node via U_τ . This allows us to find a nonlinear dynamics with respect to the input sequence $\{s_k\}$ from the dynamics of the true nodes $\{x_i(t)\}_{i=1}^N$. The emergent nonlinearity is not as special because classical (nonlinear) dynamics appears as (coarse-grained) dynamics of averaged values of the observables in the quantum system. However, the universal emulation of nonlinear dynamics by training an optimal observable in disordered (chaotic) quantum systems explained below is unique for QRC, providing an alternative paradigm to digital universal quantum computing.

Training readout weights. — We harness complex quantum dynamics in a physically natural system by utilising the reservoir computing approach. Here the signals are sampled from the QR not only at the time $k\tau$, but also

at each of the subdivided V timesteps during the unitary evolution U_τ as shown in Fig. 2, and we have named these *virtual nodes*. Thus, at each timestep k , we have NV virtual nodes in total. The virtual nodes allow us to make full use of the richness of quantum dynamics, because unitary real-time evolution is essential for nonlinearity.

Let $\{x'_{ki}\}$ ($1 \leq i \leq NV$ and $1 \leq k \leq L$) be the states of the virtual nodes in the learning phase. We also introduce $x'_{k0} = 1.0$ as a constant bias term. Suppose $\{\bar{y}_k\}_{k=1}^L$ is the target sequence, which is utilised for training. Then, what we have to do is to find linear readout weights $\{w_i\}_{i=0}^{NV}$ to obtain the output sequence

$$y_k = \sum_{i=0}^{NV} x'_{ki} w_i \quad (4)$$

such that the mean square error between the training and trained sequences is minimised. This problem is solved by using the Moore-Penrose pseudo-inverse, whereby the trained linear readout weights \mathbf{w}^{LR} are obtained easily (see Supplementary Information 1 for the details). Using \mathbf{w}^{LR} , we either obtain the output from the QR

$$y_k = \sum_{i=0}^{NV} w_i^{\text{LR}} x'_{ki}, \quad (5)$$

or equivalently, an optimal observable

$$O_{\text{trained}} \equiv \sum_{i=1}^N w_i^{\text{LR}} (I + Z_i) / 2 + w_{N+1}^{\text{LR}} I \quad (6)$$

is trained, and the output is obtained as $\langle O_{\text{trained}} \rangle$.

Specifically, as is the case in the conventional reservoir computing approach, none of the parameters of the system (Hamiltonian) require fine tuning except for the linear readout weights. Thus, we can employ any quantum system (Hamiltonian) as long as it exhibits dynamics with appropriate properties for our purpose, such as fading memory and nonlinearity. That is, as long as the QR is sufficiently rich, we can find an optimal observable O_{trained} capable of exploiting the preferred behaviour via the training (learning) process. Below we employ, as an example, the simplest quantum system, a fully connected transverse-field Ising model:

$$H = \sum_{ij} J_{ij} X_i X_j + h Z_i, \quad (7)$$

where the coupling strengths are randomly chosen such that J_{ij} is distributed randomly from $-J/2$ to $J/2$.

We start by providing several demonstrations to obtain a sense of QRC. Figure 3 shows QR performances with trained readouts for a number of benchmark tasks in the context of machine learning. The tasks include timer emulations (Fig. 3A), nonlinear autoregressive moving average (NARMA) system emulations (Fig. 3B), and Mackey-Glass (MG) time series predictions (Fig. 3C). One important property of QRC is the availability of memory for exploitation. Whether the system contains

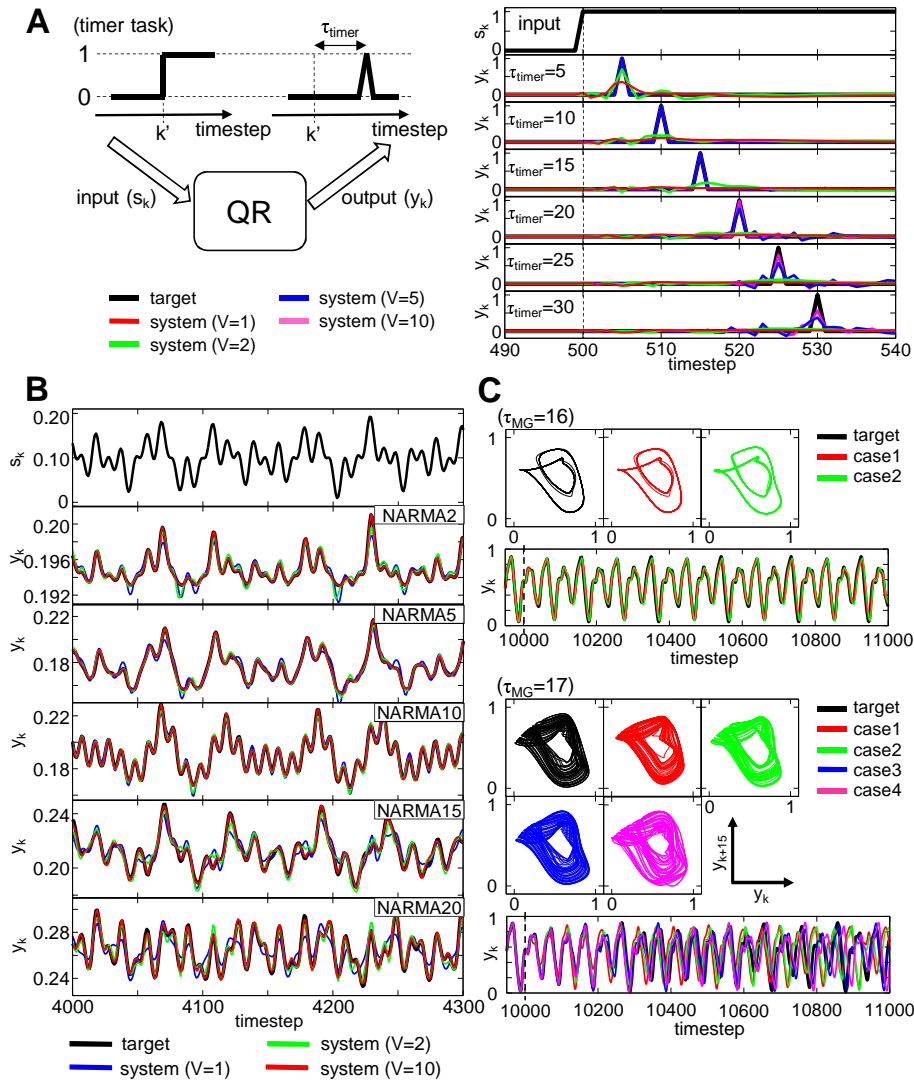


FIG. 3. **Typical performances of QR for temporal machine learning tasks.** (A) The timer task. The input is flipped from 0 to 1 at timestep k' ($= 500$) as a cue, and the system should output 1 if τ_{timer} timesteps have passed since the cue, otherwise output 0. For given τ_{timer} , the plots overlay the averaged performance of a 6-qubit QR system for each V with the target outputs. (B) The NARMA emulation task. This task requires five different NARMA systems driven by a common input stream to be emulated. The upper plot shows the input stream, and the corresponding task performances of a 6-qubit QR system for five NARMA tasks are plotted, overlaying the case for each V with the target outputs. (C) The Mackey-Glass prediction task. The performances for $\tau_{\text{MG}} = 16$ (non-chaotic) and 17 (chaotic) are shown. The trained system outputs are switched to the autonomous phase at timestep 10000. Two-dimensional plots, (y_k, y_{k+15}) , are depicted for the autonomous phase in each case. For each setting of τ_{MG} , case 1 represents the case for 6 qubits, otherwise represent the cases for 7 qubits. For all tasks, the detailed settings and analyses are provided in Supplementary Information 2.

memory can be straightforwardly evaluated by performing the timer task (see e.g., Ref. [1]). The NARMA emulation task presents a challenging problem for any computational system because of its nonlinearity and dependence on long time lags [3, 6]. The MG time series prediction is also a popular benchmark task in machine learning (e.g., Ref. [12]). Here, unlike the previous two cases, the system output is fed back as the input for the next timestep, which means that when the system generates outputs using the trained weights, it receives its own output through the feedback connections instead of

through external inputs.

The demonstrations imply that our QRC framework has sufficient potential to be used for real-world machine learning problems. In particular, in the MG prediction task, the learned model has captured the essential structure of the original attractor including the chaotic one (Fig. 3C, lower). Generally, our QR systems exhibited a tendency to improve their performance by increasing the number of qubits and the number of virtual nodes V for given τ . See Supplementary Information 2 for details and further analyses of each task.

III. PERFORMANCE ANALYSES

We perform detailed analyses on the computational capabilities of the 5-qubit QRs focusing on the two benchmark tasks of Boolean function emulations over a binary input sequence (see e.g., Refs. [11, 14]), which we name the *short-term memory* (STM) task and *parity check* (PC) task. The former task is intended to emulate a function that outputs a version of the input stream delayed by τ_B timesteps, whereas the latter is intended to emulate an τ_B -bit parity checker. Both tasks require memory to be emulated, and the PC task requires nonlinearity in addition, because the parity checker function performs nonlinear mapping. Hence, the STM task can evaluate the memory capacity of systems and the PC task can additionally evaluate the amount of nonlinearity within systems. In both tasks, we evaluate the system outputs with the target outputs for a given delay τ_B by introducing the τ_B -delay capacity $C(\tau_B)$ (denoted $C_{\text{STM}}(\tau_B)$ and $C_{\text{PC}}(\tau_B)$ for each respective capacity), which evaluates the similarity between the system and target outputs and takes the maximum value of 1 for perfect emulation and 0 for complete failure. Subsequently, the capacity C (denoted C_{STM} and C_{PC} for each respective capacity) is defined as a summation of τ_B -delay capacity over the delays. See Supplementary Information 2 for details of both tasks.

In Fig. 4A (left), $C_{\text{STM}}(\tau_B)$ is plotted as a function of τ_B for $V = 1, \dots, 50$, where $\tau\Delta = 1$ and $J/\Delta = 1.0$ are set. The abrupt decay exhibited by the curve is improved when the number of virtual nodes is increased. In Fig. 4A (middle), the STM capacity is plotted as a function of the number of virtual nodes V and the time interval $\tau\Delta$. It shows that the STM capacity becomes saturated around $V = 10$. The 5-qubit QRs with $\tau\Delta = 0.5$ and 1.0 exhibit a substantially high STM capacity ~ 20 , which is much higher than that of the ESNs of 500 nodes (see Supplementary Information 2 for details). A plot of the STM capacity as a function of τ for a fixed number of virtual nodes $V = 10$ does not exhibit monotonic behaviour as shown in Fig. 4 (right). This behaviour is understood as follows. In the limit of $\tau \rightarrow 0$, the dynamics approach an identity map and hence become less attractive, and this is more desirable to maintain the separation among different inputs. At the same time, a shorter τ implies less information is embedded in the present input setting. In the limit of larger τ , on the other hand, the input sequence is injected effectively; however, the dynamics become attractive, and the separation fades rapidly. Originating from these two competing effects, there is an optimal time interval τ for which the STM capacity is maximised.

In Fig. 4B (left), $C_{\text{PC}}(\tau_B)$ is plotted as a function of τ_B for $V = 1, \dots, 50$. Specifically, $C_{\text{PC}}(\tau_B)$ is exactly zero when $V = 1$. This clearly shows that the virtual nodes, which spatialise the real-time dynamics during the interval τ , are important to extract nonlinearity. In Fig. 4B (middle), the PC capacity is plotted as a function of the

number of virtual nodes V and the time interval $\tau\Delta$. As expected, the longer the time interval τ is, the higher the PC capacity exhibited by the QR, as shown in Fig. 4 (middle and right). This is because the true nodes are able to increase communication with the virtual nodes. The number of virtual nodes required for the saturation of the PC capacity is also increased in the case of a longer τ .

Unique properties of QRs.— Let us clarify the unique properties of the QRs in terms of the STM and PC capacities. We plot $(C_{\text{STM}}, C_{\text{PC}})$ for the 5-qubit QRs with various coupling settings in Fig. 5A, which include a restricted type of QR with one-dimensional nearest-neighbour (1DNN) couplings, i.e. $J_{ij} \neq 0$ only for $j = i + 1$. In this case, the transversal-field Ising model becomes integrable, that is, exactly solvable by mapping it into a free-fermionic model. The integrable QRs exhibit extremely longer STM but no nonlinearity. The integrable dynamics cannot exploit the entire 4^N -dimensional space; rather, it is restricted to a $2N$ -dimensional subspace. Figure 5B compares quantum chaotic and integrable dynamics. Although integrable dynamics visually behaves as though it has rich dynamics, its integrability can be appropriately detected from its computational capabilities.

In Fig. 5C, the STM and PC capacities are plotted for the QRs from $N = 2$ to $N = 7$. With the same τ and V the performance monotonically increases in terms of the number of qubits. Interestingly, if we take a sufficiently large number of virtual nodes, the PC capacity seems to increase linearly to saturate $2(N - 2)$, with N being the number of qubits (see Supplementary Information 2 for details). The 7-qubit QRs, for example, with $\tau\Delta = 2$, $J/\Delta = 2h/\Delta = 1$, and $V = 10-50$, are as powerful as the ESNs of 500 nodes with the spectral radius around 1.0. Note that even if the virtual nodes are included, the total number of nodes $NV = 350$ is less than 500.

We further investigate the effect of decoherence (noise) to validate the feasibility of QRC (see Supplementary Information 3 for the detailed analyses). We examine the decoherence by considering pure dephasing in either the z or the x directions. First, QRC is robust against decoherence; if the ratio of the decoherence rate γ and the coupling strength J is sufficiently small $J/\gamma \sim 10^{-2}$ or if τ is sufficiently long, there is no degradation of the performance. Interestingly, when the decoherence rate is increased, C_{PC} increases. This decoherence-induced enhancement of nonlinearity means that decoherence, i.e. a coupling with the environment, serves to enrich the QR dynamics. However, as the size of the true nodes is fixed, C_{STM} deteriorates because of the information leakage from the system to the unaddressable environment.

IV. DISCUSSION

The QRC approach enables us to exploit any kind of quantum system, including quantum simulators and

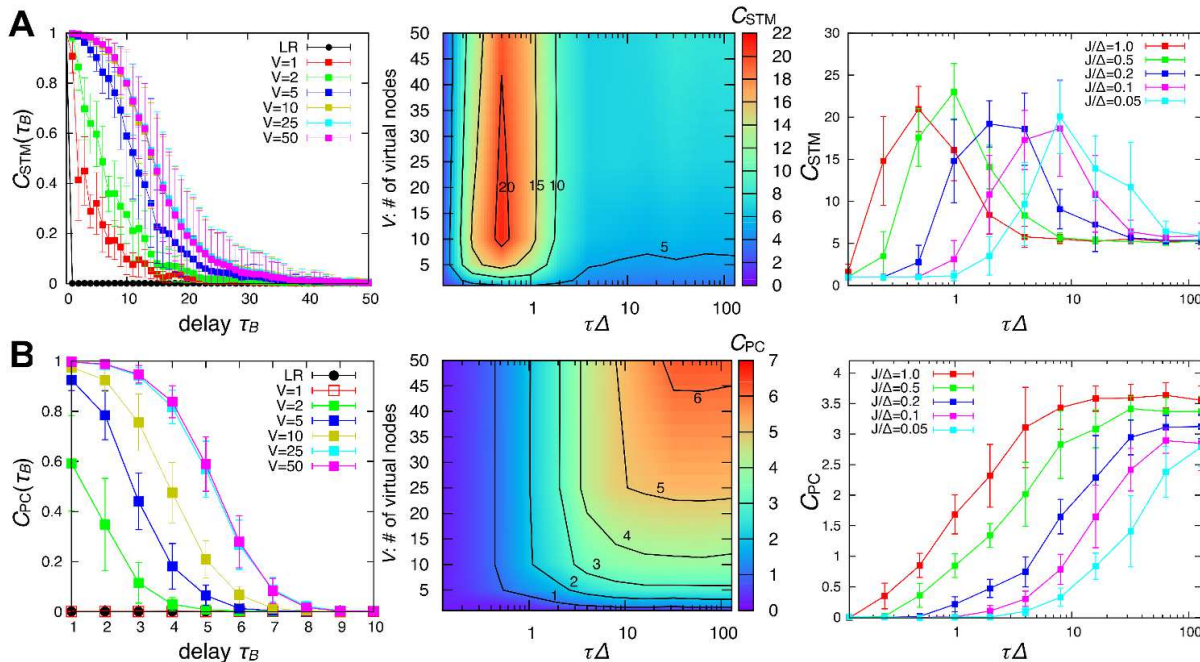


FIG. 4. **Performance analyses of the 5-qubit QRs.** (A) (left) STM curve $C_{\text{STM}}(\tau_B)$ plotted as a function of the delay τ_B for $J/\Delta = 2h/\Delta = 1$, $\tau\Delta = 1$ and $V = 1-50$. (middle) STM capacity C_{STM} plotted as a function of the number of virtual nodes V with the same QR settings for $\tau\Delta = 0.5-128$. (right) STM capacity C_{STM} plotted as a function of $\tau\Delta$ with couplings $J/\Delta = 0.05-1.0$ and $h/\Delta = 0.5$. (B) PC curve $C_{\text{PC}}(\tau_B)$ and capacity C_{PC} plotted with the same settings as (A).

quantum annealing machines, provided their dynamics are sufficiently rich and complex to allow them to be employed for information processing. For example, liquid and solid state NMR systems with nuclear and electron spin ensembles [41, 42] are favourable for implementing QRC. These systems enable us to obtain the output signals in real time via the radio-frequency coil by virtue of its huge number of ensembles. All other systems intended as quantum computers or quantum simulators, such as superconducting quantum circuits, trapped ions, and cold atoms, are also employed for QRC. Note that we have employed the simplest model, and that no optimisation of the QRs has been done yet. More study is necessary to optimise the QRs with respect to a Hamiltonian, network topology, the way of injecting the input sequences, and the readout observables.

Notwithstanding its experimental feasibility, controllability, and robustness against decoherence, the QRC framework would be also useful to analyse complex real-time quantum dynamics from an operational perspective.

The computational capabilities provide operational measures for quantum integrable and chaotic dynamics. Apparently, the STM is closely related to time correlation in many-body quantum physics and the thermalisation of closed quantum systems. Moreover, the chaotic behaviour of quantum systems has been investigated in an attempt to understand the fast scrambling nature of black holes [47, 48]. It would be intriguing to measure the computational capabilities of such black hole models. We believe that QRC for universal real-time quantum computing, which bridges quantum information science, machine learning, quantum many-body physics, and high-energy physics coherently, provides an alternative paradigm to quantum digital computing.

ACKNOWLEDGEMENTS

K.N. is supported by JST PRESTO program and KAKENHI No. 15K16076 and No. 26880010.

-
- [1] Feynman, R.P. Simulating physics with computers. *Int. J. Theor. Phys.* **21**, 467–488 (1982).
 [2] Nielsen, M.A. & Chuang, I. L. Quantum computation and quantum information. (Cambridge university press 2010).
 [3] Fujii, K. Quantum Computation with Topological Codes -From Qubit to Topological Fault-Tolerance-. Springer-Briefs in Mathematical Physics (Springer-Verlag 2015).
 [4] Shor, P.W. Algorithms for quantum computation: Discrete logarithms and factoring. *In Proceedings of the 35th Annual Symposium on Foundations of Computer Science*,

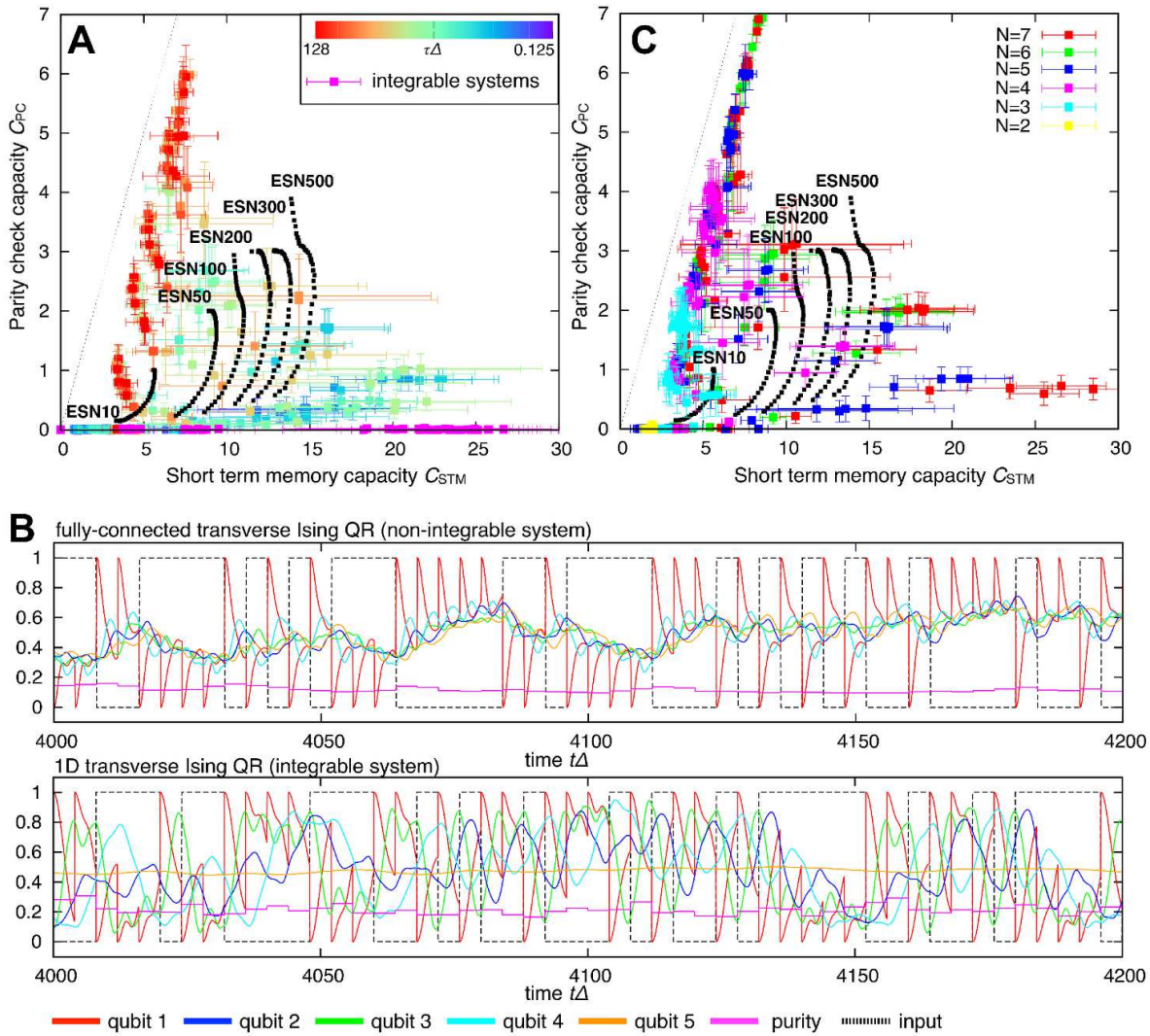


FIG. 5. **STM and PC capacities under various settings.** (A) Capacities for the 5-qubit QRs plotted with various parameters $\tau\Delta = 0.125-128$, $J/\Delta = 0.05-1.0$, $h/\Delta = 0.5$, and $V = 1-50$. Integrable cases with 1DNN couplings are shown as “integrable systems”. (B) Typical dynamics with fully connected (upper) and 1DNN couplings (lower) are shown with the signals from each qubit. The input sequence and purity, a measure of quantum coherence, are shown by dotted and solid lines, respectively. (C) QRs with $J/\Delta = 2h/\Delta = 1$ and $0.125 \leq \tau\Delta \leq 128$ for $N = 2-7$. The ESNs with 10–500 nodes are shown as references.

- 124–134 (1994).
- [5] Barends, R., et al. Superconducting quantum circuits at the surface code threshold for fault tolerance. *Nature* **508**, 500–503 (2014).
- [6] Kelly, J., et al. State preservation by repetitive error detection in a superconducting quantum circuit. *Nature* **519**, 66–69 (2015).
- [7] Cirac, J.I. & Zoller, P. Goals and opportunities in quantum simulation. *Nat. Phys.* **8**, 264–266 (2012).
- [8] Bloch, I., Dalibard, J. & Nascimbène, S., Quantum simulations with ultracold quantum gases. *Nat. Phys.* **8**, 267–276 (2012).
- [9] Georgescu, I. M., Ashhab, S., & Nori, F., Quantum simulation. *Rev. of Mod. Phys.*, **86**, 153 (2014).
- [10] Kadowaki, T. & Nishimori, H. Quantum annealing in the transverse Ising model. *Phys. Rev. E* **58**, 5355 (1998).
- [11] Farhi, E., Goldstone, J., Gutmann, S., Lapan, J., Lundgren, A. & Preda, D. A quantum adiabatic evolution algorithm applied to random instances of an NP-complete problem. *Science* **292**, 472–475 (2001).
- [12] Ronnow, T.F. et al., Defining and detecting quantum speedup. *Science* **345**, 420–424 (2014).
- [13] Boixo, S., et al. Evidence for quantum annealing with more than one hundred qubits. *Nat. Phys.* **10**, 218–224 (2014).
- [14] Morimae, T., Fujii, K., & Fitzsimons, J. F. Hardness of classically simulating the one-clean-qubit model. *Phys. Rev. Lett.* **112**, 130502 (2014).
- [15] Fujii, K., Kobayashi, H., Morimae, T., Nishimura, H., Tamate, S. & Tani S. Power of Quantum Computation with Few Clean Qubits. arXiv:1509.07276.

- [16] Fujii, K. & Tamate, S. Computational quantum-classical boundary of complex and noisy quantum systems. arXiv:1406.6932.
- [17] Merolla, P.A. *et al.*, A million spiking-neuron integrated circuit with a scalable communication network and interface. *Science* **345**, 668–673 (2014).
- [18] Jaeger, H. & Haas, H. Harnessing nonlinearity: predicting chaotic systems and saving energy in wireless communication. *Science* **304**, 78–80 (2004).
- [19] Maass, W., Natschläger, T. & Markram, H. Real-time computing without stable states: a new framework for neural computation based on perturbations. *Neural Comput.* **14**, 2531–2560 (2002).
- [20] Verstraeten, D., Schrauwen, B., D’Haene, M. & Stroobandt, D. An experimental unification of reservoir computing methods. *Neural Netw.* **20**, 391–403 (2007).
- [21] Schmidhuber, J. Deep Learning in Neural Networks: An Overview. *Neural Netw.* **61**, 85–117 (2015).
- [22] Rabinovich, M., Huerta, R. & Laurent, G. Transient dynamics for neural processing. *Science* **321**, 48–50 (2008).
- [23] Dambre, J., Verstraeten, D., Schrauwen, B. & Massar, S. Information processing capacity of dynamical systems. *Sci. Rep.* **2**, 514 (2012).
- [24] Fernando, C. & Sojakka, S. Pattern recognition in a bucket. In *Lecture Notes in Computer Science* **2801**, 588–597 (Springer, 2003).
- [25] Appeltant, L., Soriano, M.C., Van der Sande, G., Danckaert, J., Massar, S., Dambre, J., Schrauwen, B., Mirasso, C.R. & Fischer, I. Information processing using a single dynamical node as complex system. *Nat. Commun.* **2**, 468 (2011).
- [26] Woods, D. & Naughton, T.J. Photonic neural networks. *Nat. Phys.* **8**, 257 (2012).
- [27] Paquot, Y., Dupont, F., Smerieri, A., Dambre, J., Schrauwen, B., Haelterman, M. & Massar, S. Optoelectronic Reservoir Computing. *Sci. Rep.* **2**, 287 (2012).
- [28] Brunner, D., Soriano, M.C., Mirasso, C.R. & Fischer, I. Parallel photonic information processing at gigabyte per second data rates using transient states. *Nat. Commun.* **4**, 1364 (2013).
- [29] Vandoorne, K., Mechet, P., Vaerenbergh, T.V., Fiers, M., Morthier, G., Verstraeten, D., Schrauwen, B., Dambre, J. & Bienstman, P. Experimental demonstration of reservoir computing on a silicon photonics chip. *Nat. Commun.* **5**, 3541 (2014).
- [30] Stieg, A.Z., Avizienis, A.V., Sillin, H.O., Martin-Olmos, C., Aono, M. & Gimzewski, J.K. Emergent criticality in complex turing B-type atomic switch networks. *Adv. Mater.* **24**, 286–293 (2012).
- [31] Nakajima, K., Hauser, H., Kang, R., Guglielmino, E., Caldwell, D.G. & Pfeifer, R. A soft body as a reservoir: case studies in a dynamic model of octopus-inspired soft robotic arm. *Front. Comput. Neurosci.* **7**, 1–19 (2013).
- [32] Nakajima, K., Li, T., Hauser, H. & Pfeifer, R. Exploiting short-term memory in soft body dynamics as a computational resource. *J. R. Soc. Interface* **11**, 20140437 (2014).
- [33] Nakajima, K., Hauser, H., Li, T. & Pfeifer, R. Information processing via physical soft body. *Sci. Rep.* **5**, 10487 (2015).
- [34] Caluwaerts, K., Despraz, J., Işçen, A., Sabelhaus, A.P., Bruce, J., Schrauwen, B. & SunSpiral, V. Design and control of compliant tensegrity robots through simulations and hardware validation. *J. R. Soc. Interface* **11**, 20140520 (2014).
- [35] LeCun, Y., Bengio, Y., Hinton, G. Deep Learning. *Nature* **521**, 436–444 (2015).
- [36] Briegel, H.J. & De las Cuevas, G. Projective simulation for artificial intelligence. *Sci. Rep.* **2**, 400 (2012).
- [37] Paparo, G.D., Dunjko, V., Makmal, A., Martin-Delgado, M. A. & Briegel, H. J. Quantum speedup for active learning agents. *Phys. Rev. X* **4**, 031002 (2014).
- [38] Rebertrost, P., Mohseni, M. & Lloyd, S. Quantum support vector machine for big data classification. *Phys. Rev. Lett.* **113**, 130503 (2014).
- [39] Lloyd, S., Mohseni, M. & Rebertrost, P., Quantum principal component analysis. *Nat. Phys.* **10**, 631 (2014).
- [40] Adcock, J.C. *et al.*, Advances in quantum machine learning. arXiv:1512.02900.
- [41] Cory, D.G., *et al.* NMR Based Quantum Information Processing: Achievements and Prospects. *Fortschr. Phys.* **48**, 875–907 (2000).
- [42] Jones, J. A. Quantum Computing with NMR. *Prog. Nucl. Magn. Reson. Spectros.*, **59**, 91–120 (2011).
- [43] Laje, R. & Buonomano, D.V. Robust timing and motor patterns by taming chaos in recurrent neural networks. *Nat. Neurosci.* **16**, 925–933 (2013).
- [44] Hochreiter, S., Schmidhuber, J. Long short-term memory. *Neural Comput.* **9**, 1735–1780 (1997).
- [45] Atiya, A.F. & Parlos, A.G. New results on recurrent network training: Unifying the algorithms and accelerating convergence. *IEEE Trans. Neural Netw.*, **11**, 697–709 (2000).
- [46] Bertschinger, N. & Natschläger, T. Real-time computation at the edge of chaos in recurrent neural networks. *Neural Comput.* **16**, 1413–1436 (2004).
- [47] Hayden, P., Preskill, J. Black holes as mirrors: quantum information in random subsystems. *J. High Energy Phys.*, **2007**, 120 (2007).
- [48] Hosur, P., Qi, X.-L., Roberts, D. A., & Yoshida, B., arXiv:1511.04021.

SUPPLEMENTARY INFORMATION

S1. QUANTUM RESERVOIR COMPUTING

Dynamics in quantum system— The minimum unit of information in quantum physics is a quantum bit (qubit), which consists of a two-level quantum system, namely a vector in a complex vector space spanned by $\{|0\rangle, |1\rangle\}$. Let us consider a quantum system consisting of N qubits, which is described as a tensor product space of a complex vector space of two dimensions. A pure quantum state is represented by a state vector $|\psi\rangle$ in a 2^N -dimensional complex vector space. We may also consider a statistical (classical) mixture of the states of the pure state, which can be described by a $2^N \times 2^N$ hermitian matrix ρ known as a density matrix. An observable of the system is also defined as a $2^N \times 2^N$ hermitian matrix O , and its average value $\langle O \rangle$ is calculated as $\langle O \rangle := \text{Tr}[O\rho]$. Here $\text{Tr}[\cdot]$ is the matrix trace. By using the Hilbert-Schmidt inner product, the density matrix can be represented as an element \mathbf{x} on a 4^N -dimensional operator space. Here the i -th coefficient x_i of \mathbf{x} is defined by $x_i = \text{Tr}[B_i\rho]$ by using the set of N -qubit products of the Pauli operators

$\{B_i\}_{i=1}^{4^N} = \{I, X, Y, Z\}^{\otimes N}$ (where $\text{Tr}[B_i B_j]/2^N = \delta_{ij}$). Specifically, we choose the first N elements such that $B_i = Z_i$ for clarity. For a closed quantum system, the dynamics for the density matrix $\rho(t)$ is given by

$$\rho(t + \tau) = e^{-iH\tau} \rho(t) e^{iH\tau}, \quad (8)$$

where the Hamiltonian H is an $2^N \times 2^N$ hermitian matrix and defines the dynamics of the quantum system. This is rewritten as the dynamics for $\mathbf{x}(t)$:

$$\mathbf{x}(t + \tau) = U_\tau \mathbf{x}(t). \quad (9)$$

Here U_τ is a $4^N \times 4^N$ matrix whose element is defined by

$$(U_\tau)_{ji} := \text{Tr}[B_j e^{-iH\tau} B_i e^{iH\tau}]/2^N. \quad (10)$$

Owing to the unitarity of the dynamics $e^{-iH\tau} (e^{-iH\tau})^\dagger = I$, we have $U_\tau U_\tau^\dagger = I$. If the system is coupled to an external system for a measurement and/or a feedback operation, the time evolution (for the density matrix) is not given by the conjugation of the unitary operator $e^{-iH\tau}$; instead, it is generally given by a complete positive trace preserving (CPTP) map \mathcal{D} for the density matrix ρ . Even in such a case, the dynamics is linear, and hence the time evolution for $\mathbf{x}(t)$ is given in a linear form:

$$\mathbf{x} \rightarrow W\mathbf{x} \quad (11)$$

where the matrix element is defined

$$W_{ji} := \text{Tr}[B_j \mathcal{D}(B_i)]/2^N. \quad (12)$$

Let us consider the replacement of the state on the first qubit for the injection of the input sequence. The density matrix ρ of the system is transformed as

$$\rho \rightarrow \rho_{s_k} \otimes \text{Tr}_1[\rho], \quad (13)$$

where Tr_1 indicates the partial trace with respect to the first qubit. The above action of the k th input on the state $\mathbf{x}(t)$ is again denoted by a matrix S_k . After the injection, the system evolves under the Hamiltonian H for a time interval τ . Thus, the time evolution of the state for a unit timestep is given by

$$\mathbf{x}(k\tau) = U_\tau S_k \mathbf{x}((k-1)\tau). \quad (14)$$

Training— The time interval τ is subdivided into V and at each time $t + v(\tau/V)$ with an integer $1 \leq v \leq V$ the signals $x'_i(t + v(\tau/V)) = \text{Tr}[Z_i \rho(t + v(\tau/V))]$ are sampled. These time multiplexed signals are denoted by x'_{ki} with $i = n + vN$ with integers $1 \leq n \leq N$ and $0 \leq v \leq V$, x'_{ki} , which means the signal of the n th qubit at time $t = k\tau + v(\tau/V)$, i.e. $x'_{ki} := x'_i(k\tau + v(\tau/V))$.

Let $\{\bar{y}_k\}_{k=1}^L$ be the target sequence, which is utilized for the training. In the reservoir computing approach, learning of a nonlinear function $y_m = f(\{s_k\}_{k=1}^m)$, which emulates the target sequence $\{\bar{y}_k\}$, is executed by training the linear readout weights of the reservoir states such that the mean square error

$$\frac{1}{L} \sum_{k=1}^L (y_k - \bar{y}_k)^2 \quad (15)$$

is minimised. This problem corresponds to solving the following equations:

$$\bar{\mathbf{y}} = \mathbf{X}\mathbf{w}, \quad (16)$$

where $\{x'_{ki}\}$, $\{\bar{y}_k\}_{k=1}^L$, and $\{w_i\}_{i=0}^{NV}$ are denoted by a $L \times (NV + 1)$ matrix \mathbf{X} , and column vectors $\bar{\mathbf{y}}$ and \mathbf{w} , respectively. Here we assume that the length of the training sequence L is much larger than the total number of the nodes $NV + 1$ including the bias term. Thus, the above equations are overdetermined, and hence the weights that minimise the mean square error are determined by the Moore-Penrose pseudo-inverse $\mathbf{X}^+ := (\mathbf{X}^\top \mathbf{X})^{-1} \mathbf{X}^\top$ ($(NV + 1) \times L$ matrix) of \mathbf{X} as follows:

$$\mathbf{w}^{\text{LR}} := \mathbf{X}^+ \bar{\mathbf{y}}. \quad (17)$$

S2. EXPERIMENTAL SETTINGS AND EXTENDED ANALYSES

This section describes detailed settings for the task experiments mentioned in the main text and provides extended analyses as supporting information. We have maintained the notation for symbols used in the main text.

The timer task— The timer task is one of the simplest yet most important benchmark tasks to evaluate the memory capacity of a system (see, e.g., Ref. [1]). As explained in the main text, our goal for the first demonstration of QRC was to emulate the function of a timer (Fig. 3A in the main text). The I/O relation for a timer can be expressed as follows:

$$s_k = \begin{cases} 1 & (k \geq k') \\ 0 & (\text{otherwise}) \end{cases}$$

$$y_k = \begin{cases} 1 & (k = k' + \tau_{\text{timer}}) \\ 0 & (\text{otherwise}), \end{cases}$$

where k' is a timestep for launching the cue to the system, and τ_{timer} is a delay for the timer. Our aim was to emulate this timer by exploiting the QR dynamics generated by the input projected to the first qubit in the QR system. To perform this task, the system has to be able to ‘recognise’ the duration of time that has passed since the cue was launched. This clearly requires memory.

A single experimental trial of the task consists of 800 timesteps, where the first 400 timesteps are discarded as initial transients. At timestep 500, the input is switched from 0 to 1 (i.e. $k' = 500$), and the system continues to run for another 300 timesteps. For the training procedure, using a 6-qubit QR system with $\tau\Delta = 1$, we iterated this process over five trials, starting from different initial conditions, and collected the corresponding QR time series for each timestep from timestep 400 to timestep 800 as training data. We optimised the linear readout weights using these collected QR time series with a linear regression to emulate the target output for the given delay τ_{timer} and the setting of the number of virtual

nodes V in QR systems. We evaluated the performance of the system with the optimised weights by running five additional trials (evaluation trials) and compared the system outputs to the target outputs in the time region from timestep 400 to timestep 800.

The plot in Fig. 3A in the main text is obtained by averaging the system output using the evaluation trials for each timestep. We can clearly observe that increasing the number of V improves the performance, which means that the amount of memory available for exploitation has also increased. In particular, when $V = 5$ and 10, the system outputs overlap with the target outputs within a certain delay, which clearly demonstrates that our QR system is capable of embedding a timer. By increasing the delay timesteps τ_{timer} , a gradual decline in performance becomes obvious, thereby expressing the limitation of the amount of memory that can be exploited within the QR dynamics. It is interesting to note that while the systems are highly disordered, we can find an observable O_{trained} or a mode at which the wave function of the system is focused after a desired delay time τ_{timer} . This is very useful as a control scheme for engineering quantum many-body dynamics.

Here, we aim to analyse the performance of the timer task further. We prepared 10 different 6-qubit QR systems, whose coupling strengths are assigned differently, and for each setting of (τ_{timer}, V) , we iterated the experimental trials as explained above over these 10 different systems. To effectively evaluate the system's performance against the target outputs \bar{y}_k , given the setting of τ_{timer} , we defined a measure $C(\tau_{\text{timer}})$, which is expressed as

$$C(\tau_{\text{timer}}) = \frac{\text{cov}^2(y_k, \bar{y}_k)}{\sigma^2(y_k)\sigma^2(\bar{y}_k)},$$

where $\text{cov}(x, y)$ and $\sigma(x)$ express the covariance between x and y and the standard deviation of x , respectively. In short, this measure evaluates the association between two time series, and takes a value from 0 to 1. If the value is 1, it means that the system outputs and the target outputs completely overlap, which implies that the learning was perfect. At the other extreme, if the value is 0, it implies that the learning completely failed. Evaluation trials were used to actually calculate this measure. Now, we further define a measure, capacity C , which is expressed as a simple summation of $C(\tau_{\text{timer}})$ over the entire delay,

$$C = \sum_{\tau_{\text{timer}}=0}^{\tau_{\text{timer}}^{\text{max}}} C(\tau_{\text{timer}}),$$

where $\tau_{\text{timer}}^{\text{max}}$ is set to 300 in our experiments.

By using these two measures, $C(\tau_{\text{timer}})$ and C , we evaluated the performance of the timer tasks of 6-qubit QR systems. Figure 6 plots the results. Figure 6A clearly indicates that larger values of V can perform the timer task reliably for a longer delay, which shows a characteristic

curve for each setting of V . This point is also confirmed by checking the plot of C according to the value of V , where C increases almost linearly with an increase in V (see Fig.6B). These results are consistent with the result demonstrated in the main text.

The NARMA task— As explained in the main text, the emulation of NARMA systems is a challenge for machine learning systems in general because it requires nonlinearity and memory [2]. Thus, the emulation task has been a benchmark for evaluating the amount of nonlinearity and memory to be exploited in the system [3–10]. The first NARMA system that we used is the following second-order nonlinear dynamical system:

$$y_{k+1} = 0.4y_k + 0.4y_k y_{k-1} + 0.6s_k^3 + 0.1. \quad (18)$$

This system was introduced in Ref. [3] and used, for example, in Ref. [7–10]. For descriptive purposes, we refer to this system as NARMA2. The second system is the following nonlinear dynamical system that has an order of n :

$$y_{k+1} = \alpha y_k + \beta y_k \left(\sum_{j=0}^{n-1} y_{k-j} \right) + \gamma s_{k-n+1} s_k + \delta, \quad (19)$$

where $(\alpha, \beta, \gamma, \delta)$ are set to $(0.3, 0.05, 1.5, 0.1)$, respectively. Here, n is varied using the values of 5, 10, 15, and 20, and the corresponding systems are named NARMA5, NARMA10, NARMA15, and NARMA20, respectively. In particular, NARMA10 with this parameter setting was introduced in Ref. [3] and widely used (see, e.g., Refs. [4, 5, 7–10]). Here, according to an input stream, the system should simultaneously emulate five NARMA systems (NARMA2, NARMA5, NARMA10, NARMA15, and NARMA20), which we refer to as multitasking. These tasks appear as a second demonstration of QRC in the main text (Fig. 3B in the main text). Here, we explain the experimental procedures in detail and present extended analyses for these tasks.

We used a superimposed sine wave for the input to the NARMA systems, which is expressed as follows:

$$s_k = 0.1 \left(\sin\left(\frac{2\pi\alpha k}{\lambda}\right) \sin\left(\frac{2\pi\beta k}{\lambda}\right) \sin\left(\frac{2\pi\gamma k}{\lambda}\right) + 1 \right),$$

where $(\alpha, \beta, \gamma) = (2.11, 3.73, 4.11)$ and $T = 100$. Note that s_k is in the range $[0, 0.2]$ with the aim of stabilising the behaviour of the NARMA systems (to prevent divergence). Similar types of input sequences for NARMA systems can be found in Ref. [7–10]. The input range is rescaled to $[0, 1]$ when projected to the first qubit of the QR system. The experimental trial consists of 5000 timesteps, where the first 1000 timesteps are used for the washout, the following 3000 timesteps are used for the training phase, and the final 1000 timesteps are used for the evaluation phase. Note that when the input is a superimposed sine wave, we should be careful to prevent the same input and target output time series in the training phase from appearing again in the evaluation phase,

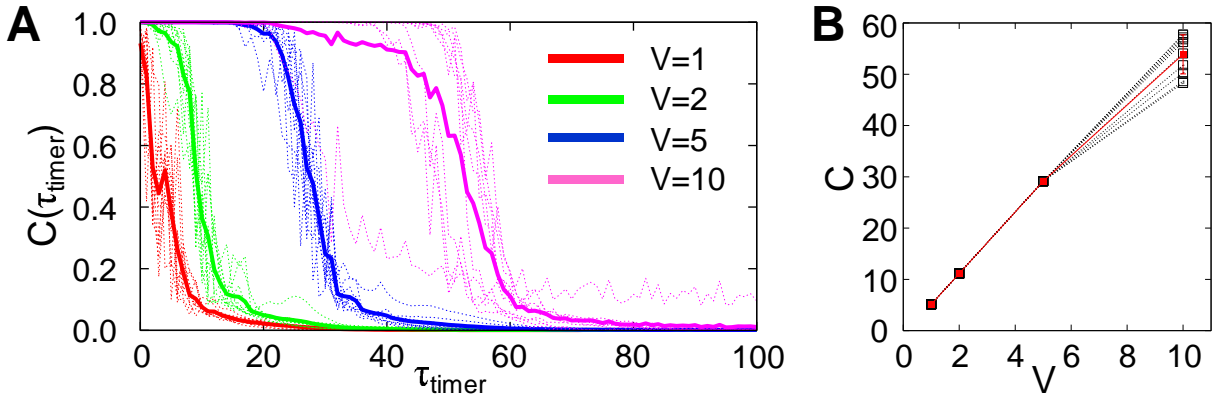


FIG. 6. **Analyses of the memory capacity based on $C(\tau_{\text{timer}})$ and C for a 6-qubit QR system.** (A) Plot showing $C(\tau_{\text{timer}})$ according to τ_{timer} for $V = 1, 2, 5,$ and 10 . For each setting of V , 10 different 6-qubit QR systems are prepared and for each system, the average of $C(\tau_{\text{timer}})$ is calculated using five trials according to τ_{timer} (dashed lines: the cases for 10 different QR systems are overlaid), and the averaged values for these averaged $C(\tau_{\text{timer}})$ over 10 different QR systems are overlaid as solid lines. (B) Plot of C as a function of V . Similar to (a), the averaged C for each different QR system for each number of V is overlaid as a dashed line and the averaged values for these averaged C over 10 different QR systems are overlaid as solid lines. The error bars represent the standard deviations.

because this would not enable us to characterise the generalisation capability of the system effectively. Our setting of the length of the training and evaluation phases is confirmed to be safe on this point. By collecting the QR time series and the corresponding target outputs for each task in the training phase, we train the linear readouts for five outputs, which correspond to the five target NARMA systems, by using the scheme explained in the main text. The trained linear readouts are used to generate system outputs for the evaluation phase.

Figure 3B in the main text plots the input sequence and the corresponding task performance of our 6-qubit QR system with $\tau\Delta = 1$ with trained readout by varying the number of V . We can clearly observe that by increasing the number of V , the performance improves, such that when $V = 10$, the system outputs almost overlap with the target outputs. The contribution of the QR system is characterised explicitly by comparing the task performance with a simple linear regression (LR) model, $y_{k+1} = w'_1 \times s_k + w'_0$, where w'_0 and w'_1 are trained using the same time series as in the training phase. Note that this corresponds to the case in which no QR system is available, and only the raw input remains for LR. This comparison enables us to conclude that, for any system performance exceeding that of this model, the QR system has contributed to the emulation task [7–11].

We evaluate the performance of the system output in the evaluation phase by calculating the normalised mean squared error (NMSE) with the target output:

$$NMSE = \frac{\sum_{k=L+1}^{M-L} (\tilde{y}_{k+1} - y_{k+1})^2}{\sum_{k=L+1}^{M-L} \tilde{y}_{k+1}^2}, \quad (20)$$

where L represents the timesteps for the washout and training phase, of which the duration is 4000 timesteps in this experiment, and M is the timesteps for the evalu-

ation phase, which requires 1000 timesteps. Table I lists the NMSE for each of the experimental conditions. We can confirm that our 6-qubit QR system outperforms the LR system in any setting of V for each NARMA task, which implies that the QR system has contributed to the task performance. Furthermore, we can see that by increasing the number of V , the performance improves in all the NARMA tasks, which is consistent with the plots presented in Fig. 3B in the main text.

Here we aim to further analyse the information processing capacity of our QR system based on the NARMA tasks. We adopt the same task settings as for the previous case except for the input settings. The input stream is generated by using white noise with a range of $[0, 0.2]$ for the same reason as in the previous experiment, rather than using a superimposed sine wave. This choice of input stream is commonly used [3–5] and is determined not to add additional temporal coherence originating from external input to the system, and to evaluate the pure computational power only contributed by the QR systems. As this input setting perceptibly complicates the performance evaluation, we quantified the task performance in terms of NMSE. For each NARMA task, we tested the relevance of τ and V in terms of the task performance and varied them for $\tau\Delta = 1, 2, 4, 8, 16, 32, 64,$ and 128 , and $V = 1, 2, 5, 10, 25,$ and 50 , respectively. Using a 5-qubit QR system, 20 samples of the QRs were randomly generated and for each $(\tau\Delta, V)$ setting, the average values of NMSEs were obtained.

The performance of the QR systems was characterised by again using the previously mentioned LR system for comparison. Furthermore, we used a conventional echo state network (ESN) as a candidate for the standard machine learning system and used it to compare our task performance. The basic settings of the ESN are described in a later section (“Echo state network settings for com-

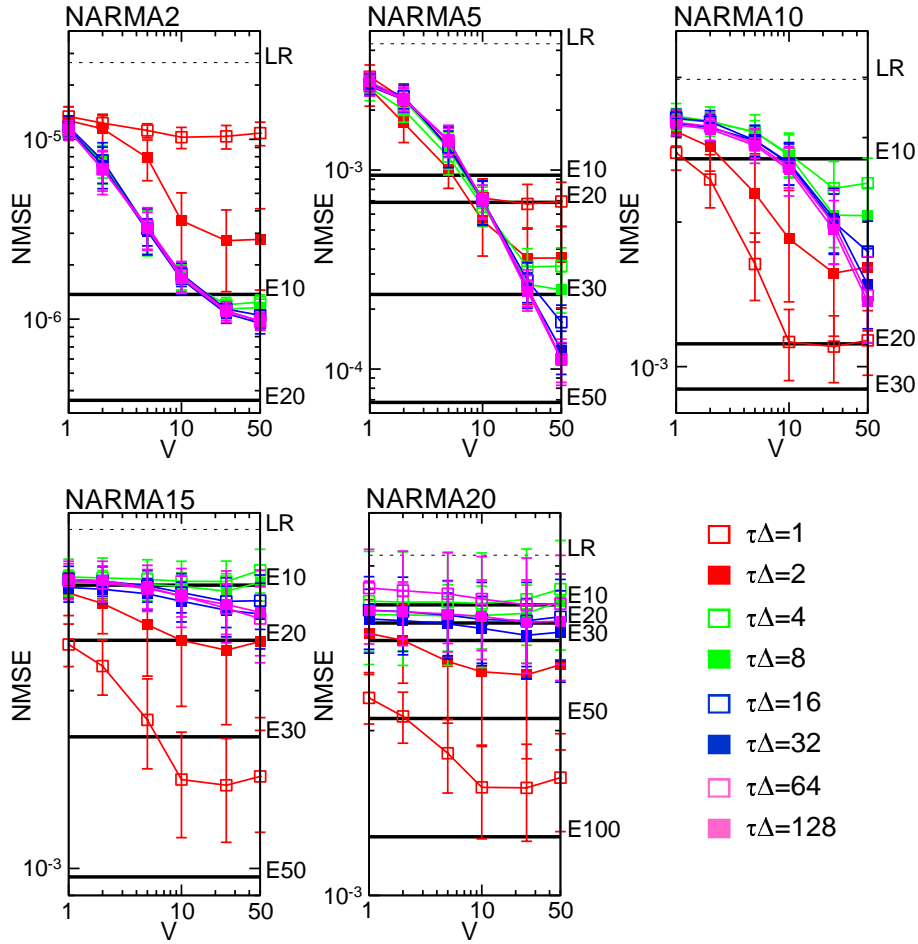


FIG. 7. **Performance of 5-qubit QR systems with several $\tau\Delta$ settings for the NARMA tasks with a random input stream.** For each plot, the vertical and horizontal axes show the NMSE and the number of virtual nodes V , respectively, and both axes are in logarithmic scales. The error bars show the standard deviations. For comparisons, the dashed line shows the performance of an LR system in terms of NMSE, and the solid lines show the performance of an ESN with N nodes (e.g. “E10” represents the performance of ESN with 10 nodes). See text for details on analyses and experimental procedures.

parisons”) of this material. To allow for fair comparisons, 100 samples of ESN with N nodes were generated by assigning the same NARMA tasks with the same experimental settings explained above, and the average values of NMSEs for the ESN were obtained (by varying the spectral radius of the ESN internal weight matrix from 0.05 to 1.95 in increments of 0.1; the case of the smallest NMSE, which provided the best performance, was used for comparison). The number of nodes N was varied for $N = 10, 20, 30, 50$, and 100 for each NARMA task.

Figure 7 depicts the results for the performance of the 5-qubit QR system for the NARMA tasks with a random input stream. First, we can see that for all the NARMA tasks, our 5-qubit QR system outperformed the LR system, which means that the QR system actually contributed to the task performance. In general, we can confirm that the increase in the number of the virtual nodes V leads to an improved performance. The effect of the number of $\tau\Delta$ on the task performance depends on the type of task. For the NARMA2 and NARMA5

tasks, an increase in the number of $\tau\Delta$ tends to improve the performance. In particular, for the NARMA5 task, when $V = 50$ and $\tau\Delta = 128$, the 5-qubit QR system performed at a level in between the performance of the ESN with $N = 30$ and $N = 50$ (see Fig. 7). For NARMA10, NARMA15, and NARMA20, this tendency does not hold in general and the use of a small number of $\tau\Delta$ was found to improve the performance. In particular, for the NARMA20 task, when $\tau\Delta = 1$ and $V > 5$, the 5-qubit QR system performed at a level in between the performance of the ESN with $N = 50$ and $N = 100$ (see Fig. 7). Interestingly, this implies that the 5-qubit QR system can deliver a performance similar to that of an ESN with fewer computational nodes (e.g. when $\tau\Delta = 1$ and $V = 5$, the 5-qubit QR system has 25 computational nodes and the performance exceeds that of an ESN with 50 nodes). These outcomes of the task performance are induced by the balancing of memory and nonlinearity, which can be exploited by the system and which is required to perform the task; this is closely related to the

TABLE I. Performance of the System using the superimposed sine wave. Error (NMSE) for NARMA tasks.

Task	System	Error (NMSE)
NARMA2	LR	1.7×10^{-5}
	QR ($V = 1$)	1.0×10^{-5}
	QR ($V = 2$)	4.7×10^{-6}
	QR ($V = 5$)	1.7×10^{-7}
NARMA5	LR	3.0×10^{-3}
	QR ($V = 1$)	4.6×10^{-4}
	QR ($V = 2$)	7.1×10^{-5}
	QR ($V = 5$)	2.8×10^{-5}
NARMA10	LR	2.6×10^{-3}
	QR ($V = 1$)	2.0×10^{-4}
	QR ($V = 2$)	9.2×10^{-5}
	QR ($V = 5$)	3.0×10^{-5}
NARMA15	LR	2.7×10^{-3}
	QR ($V = 1$)	6.7×10^{-4}
	QR ($V = 2$)	3.1×10^{-4}
	QR ($V = 5$)	1.2×10^{-4}
NARMA20	LR	2.3×10^{-3}
	QR ($V = 1$)	1.2×10^{-3}
	QR ($V = 2$)	2.6×10^{-4}
	QR ($V = 5$)	1.3×10^{-4}
	QR ($V = 10$)	3.8×10^{-5}

results mentioned in the main text. Further analyses will be included in our future work.

The Mackey-Glass prediction task— Chaotic attractor learning is a popular test for learning dynamical systems [12, 13]. One of the well-known systems used for the target of learning is the Mackey-Glass (MG) delay differential equation

$$\dot{y}(t) = \frac{\alpha y(t - \tau_{\text{MG}})}{1 + y(t - \tau_{\text{MG}})^\beta} - \gamma y(t),$$

where the parameters are set to $\alpha = 0.2$, $\beta = 10$, and $\gamma = 0.1$. The system has a chaotic attractor if $\tau_{\text{MG}} > 16.8$. In the majority of studies, $\tau_{\text{MG}} = 17$ is used, which yields a chaotic attractor. In our experiments, we also used this parameter setting of $\tau_{\text{MG}} = 17$. Additionally, we used the case of $\tau_{\text{MG}} = 16$ for comparison, as this setting does not exhibit chaos.

The discrete time version of the MG system is often used to prepare the training sequences [12] through

$$y_{k+1} = y_k + \sigma \left(\frac{0.2y_{k-\frac{\tau_{\text{MG}}}{\sigma}}}{1 + y_{k-\frac{\tau_{\text{MG}}}{\sigma}}^{10}} - 0.1y_k \right),$$

with a step size of $\sigma = 1/10$ and then sub-sampled by 10. One step from k to $k + 1$ in the resulting sequences corresponds to a unit time interval $[t, t + 1]$ of the original continuous system. In our numerical experiments, the

target time series is linearly scaled to $[0, 1]$ and used in the actual experiments.

For each setting of τ_{MG} , we generated the above system for a while as a washout and then a length of 12000 timesteps (already sub-sampled) was collected for the experiment. We used 10000 timesteps for the training phase and the remaining 2000 timesteps for the evaluation phase. The task was to train the QR system by using these training sequences, which after training should re-generate the corresponding chaotic or non-chaotic attractors.

Because this task requires feedback to the system, the training procedure is different from the previous cases. During the training phase, we clamped the feedback from the system output, and provided the target outputs as inputs, which means we set $s_{k+1} = \bar{y}_k$. Thus, the training phase was carried out with an open loop, such that the system was forced into the desired operative state by the target signals (this approach is typically referred to as *teacher forcing*). The robustness of the learning was improved by adding a slight amount of noise in the range of $[-\sigma, \sigma]$ in the training phase. When the evaluation phase started, we switched the inputs to the system output generated by the trained readout weights (this phase is expressed as the autonomous phase in Fig. 3C in the main text) and checked whether the system was able to embed the corresponding MG system.

Figure 3C in the main text depicts the typical task performance of 6- and 7-qubit QR systems. When $\tau_{\text{MG}} = 16$, the system outputs overlap the target outputs, which implies successful emulations. When $\tau_{\text{MG}} = 17$, our systems tend to remain relatively stable in the desired trajectory for about 200 steps after switching from the teacher forced condition, and then start to deviate to a perceptibly large extent. Furthermore, checking a two-dimensional plot by plotting points (y_k, y_{k+15}) , it appears that the learned model has captured the essential structure of the original attractor. In both tasks, the 7-qubit QR systems generally outperformed the 6-qubit QR systems. Table II summarises the experimental settings and the prediction errors for the QR system used in the main text. We calculated the errors in NMSE by using the entire time series in the evaluation phase.

TABLE II. Experimental settings and prediction errors (NMSE) for the Mackey-Glass prediction tasks in the main text.

τ_{MG}	Case	Qubit	$\tau\Delta$	Noise strength (σ)	Error (NMSE)
16	1	6	3	1.0×10^{-4}	4.7×10^{-3}
	2	7	2	1.0×10^{-4}	3.9×10^{-3}
17	1	6	3	1.0×10^{-4}	1.6×10^{-1}
	2	7	3	1.0×10^{-4}	2.5×10^{-2}
	3	7	4	1.0×10^{-5}	4.9×10^{-2}
	4	7	2	1.0×10^{-5}	1.7×10^{-2}

We tested whether the trained network indeed generates a chaotic time series by empirically estimating the

largest Lyapunov exponent of the network-generated output signal by using a procedure similar to that introduced in Ref. [13]. For the trained network, we analysed the previous four cases (case 1 ~ 4) in $\tau_{MG} = 17$ setting. When the network was switched from the teacher forcing condition to the closed-loop mode at timestep 10000, the reservoir signals were perturbed by a uniform noise vector, and the network was left running freely, on this occasion starting from the perturbed state for the entire 2000 steps of the evaluation phase, and the resulting output sequence was recorded. The exponential divergence rate λ between this perturbed sequence y'_k and the original sequence y_k was estimated by computing

$$d_k = \|[y_{10001+k} \dots y_{10017+k}] - [y'_{10001+k} \dots y'_{10017+k}]\|,$$

$$\lambda = \frac{\log(d_{500}) - \log(d_0)}{500},$$

where the subsequent 17 timesteps that are used for the computation of d_k were chosen because they correspond to approximately one full “loop” of the attractor. Figure 8 plots the behaviour of d_k for four cases. We can see that all four cases have a positive λ value, which implies that their output sequences are chaotic.

The short-term memory task and the parity check task— In this section, we discuss the experimental settings of the tasks mentioned in the main text (in the section “Performance analyses”): the short-term memory (STM) task and the parity check (PC). These tasks are the emulation tasks of the Boolean functions, and are also popular benchmark tasks to evaluate computational capabilities [11, 14]. Following the notation defined in the main text, the function for the STM task can be expressed as follows:

$$y_k = s_{k-\tau_B},$$

where s_k is a binary sequence and τ_B represents the delay. The function for the PC task is expressed as follows:

$$y_k = Q\left(\sum_{m=0}^{\tau_B} s_{k-m}\right),$$

$$Q(x) = \begin{cases} 0 & (x \equiv 0 \pmod{2}) \\ 1 & (\text{otherwise}). \end{cases}$$

We investigated both tasks thoroughly by applying a random input sequence for the tasks such that there is no external source to provide temporal coherence to the system. In these tasks, one trial consists of 5000 timesteps. The first 1000 timesteps are discarded, the next 3000 timesteps are used for training, and the last 1000 timesteps are used for system evaluation. We evaluated the system performance with the target output for each given τ_B by using the measure known as τ_B -delay capacity $C(\tau_B)$ expressed as

$$C(\tau_B) = \frac{\text{cov}^2(y_k, \bar{y}_k)}{\sigma^2(y_k)\sigma^2(\bar{y}_k)}.$$

In the main text, τ_B -delay capacities for the STM task and the PC task are termed τ_B -delay STM capacity $C_{STM}(\tau_B)$ and τ_B -delay PC capacity $C_{PC}(\tau_B)$, respectively. Note that, in the analyses, to reduce a bias due to the effect of the finite data length, we have subtracted $C(\tau_B^{\max})$ from $C(\tau_B)$, where τ_B^{\max} is a substantially long delay. The capacity C is defined as

$$C = \sum_{\tau_B=0}^{\tau_B^{\max}} C(\tau_B),$$

where τ_B^{\max} was 500 throughout our experiments. The capacities for the STM task and the PC task are referred to as the STM capacity C_{STM} and the PC capacity C_{PC} , respectively. For each task, 20 samples of the QRs were randomly generated, and the average values of the τ_B -delay capacities and the capacities were obtained.

Echo state network settings for comparisons— We further characterised the computational power of our QR system by comparing its task performance with that of a conventional echo state network (ESN) [12, 13, 15, 16] (the comparisons of ESN performance with that of our systems appear in the section “Unique properties of QRs” in the main text and also in the analyses of the NARMA tasks demonstrated above). The ESN is a type of recurrent neural network, which has N internal network units, input units, and output units. Activation of the i th internal unit at timestep k is x_k^i ($i = 1, \dots, N$). We used the same I/O setting for the ESN as with our system for each task concerned to enable us to efficiently and directly compare the performance. The number of trials, the lengths of the washout, training, and evaluation phases, and the evaluation procedures are also kept the same. The connection weights for the $N \times N$ internal network connecting the i th unit with the j th unit are denoted as w_{ij} , and the input weights proceeding from the input unit into the i th internal unit are denoted as w_{in}^i . The readout weights w_{out}^i proceed from N internal units and one bias to the output unit (where $x_k^0 = 1$ and w_{out}^0 for a bias term). The readout weights w_{out}^i are trained using the procedure explained in the main text for each task; the internal weights w_{ij} and the input weights w_{in}^i are randomly assigned from the range $[-1.0, 1.0]$ and fixed beforehand. The activation of the internal units and the output unit are updated as

$$x_k^i = f\left(\sum_{j=1}^N w_{ij}x_{k-1}^j + w_{in}^i s_k\right),$$

$$y_k = \sum_{i=0}^N w_{out}^i x_k^i,$$

where f is a tanh function. It is reported that the computational power of ESN can be well characterised by the spectral radius of the internal connection weight matrix [4, 12, 13, 15, 16]. In each comparative experiment, by incrementally varying the spectral radius, we observed

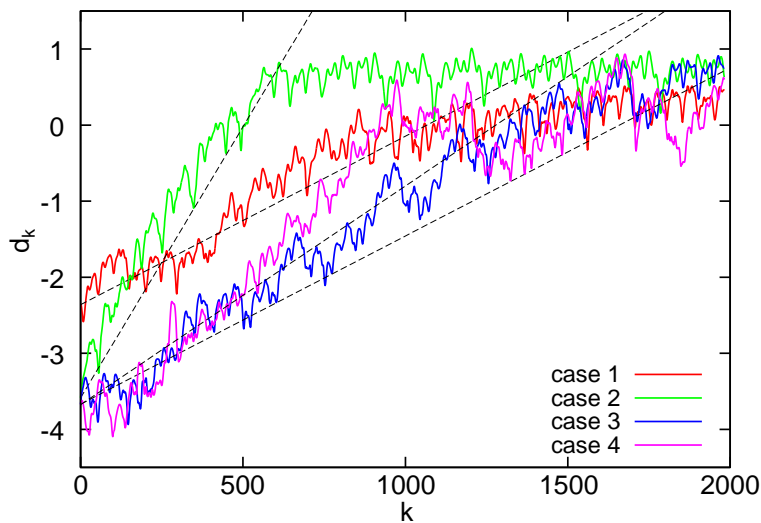


FIG. 8. **Plot showing the time series of d_k .** The results for case 1 \sim 4 are overlaid. Note that the vertical axis is in a logarithmic scale. The estimated largest Lyapunov exponent λ is 0.0022, 0.0071, 0.0022, and 0.0029 for case 1, 2, 3, and 4, respectively.

the ESN performance. Detailed experimental conditions are given for each of these comparisons.

Here we present the ESN settings for the comparisons with QR systems appeared in the section “Unique properties of QRs” in the main text. The experimental settings including the length of training and evaluation phases are kept the same with the QR system for the fair comparison. For the random binary input sequence, we adopted two cases. In the first case (Case I), we changed the actual input value to “-1” only if $s_k = 0$. For the second case (Case II), we directly projected the $\{0, 1\}$ -binary state input s_k to the internal network units. In the ESN, if $s_k = 0$, the internal units receive no external input, and therefore, are expected to introduce an asymmetry into the network performance. We tested these two cases (Case I and Case II) in Fig. 9. As can be seen from the plot, both cases show different modalities of performances in terms of C_{PC} and C_{STM} , which are due to the asymmetry introduced by the input settings. We have presented the results for Case I in the main text but the same explanations hold for both cases.

S3. DETAILED ANALYSES OF QR CHARACTERISTICS

Scaling of STM and PC capacities— Here we further investigate the scaling of the STM and PC capacities against the number of the qubits N in the QRs. In Fig. 10, the STM and PC capacities are plotted against the number of qubits for the virtual nodes $V = 1, 2, 5, 10, 25$, and 50. First, both capacities monotonically increase in the number of the qubits N and the virtual nodes V . Thus, by increasing the time resolution and size of the QR, we can enhance its computational capability. The STM capacity is improved by increasing the

number of virtual nodes V especially for optimally chosen time intervals τ . The improvement saturates around $V = 10$. The scaling behaviour of the STM capacity seems to be different for $N = 2-4$ and $N = 4-7$ when the virtual nodes are introduced. For optimally chosen time intervals, the STM capacity seems to increase linearly in terms of the number of qubits.

The PC capacity also increases in terms of the number of virtual nodes V , but its saturation highly depends on the choice of the time interval τ . For a short interval $\tau\Delta = 1$, the PC capacity saturates around $V = 10$. However, for $\tau\Delta = 128$, it seems not to saturate even with $V = 50$. In any case, the PC capacity seems to increase linearly in terms of the number of the qubits N . Interestingly, at the large τ and large V limits, the PC capacity saturates the line defined by $C_{PC} = 2(N - 2)$. The origin of this behaviour is completely unknown at this moment.

Robustness against imperfections— Here we investigate noise tolerance of QRC. We consider two types of noise: the first is decoherence, which is introduced by an undesired coupling of QRs with the environment, thereby resulting in a loss of quantum coherence, and the other is a statistical error on the readout signals from QRs. The former is more serious because quantum coherence is, in general, fragile against decoherence, which is the most difficult barrier for realisations of quantum information processing.

We employ the dephasing noise as decoherence, which is a simple yet experimentally dominant source of noise. In the numerical simulation, the time evolution is divided into a small discrete interval δt , and qubits are exposed to the single-qubit phase-flip channel with probability $(1 -$

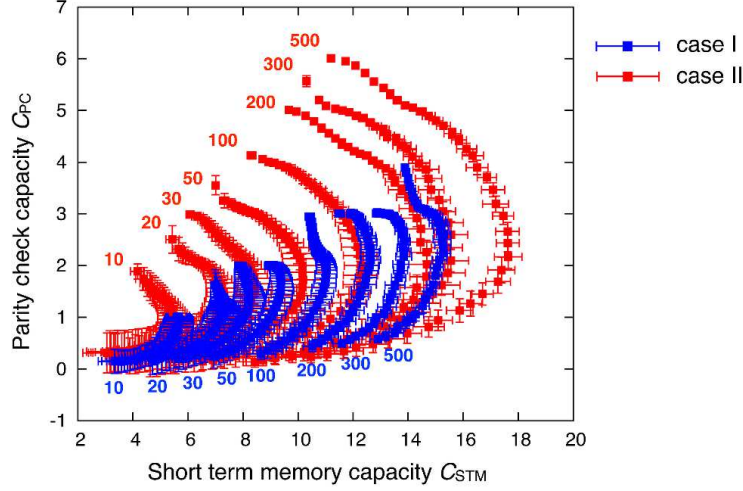


FIG. 9. Capacities (C_{STM}, C_{PC}) of the ESNs with two types of input sequence. Case I and II represent input type with $\{-1, 1\}$ (coloured blue) and with $\{0, 1\}$ (coloured red), respectively. Plots show the results for the spectral radius from 0.05 to 2.00.

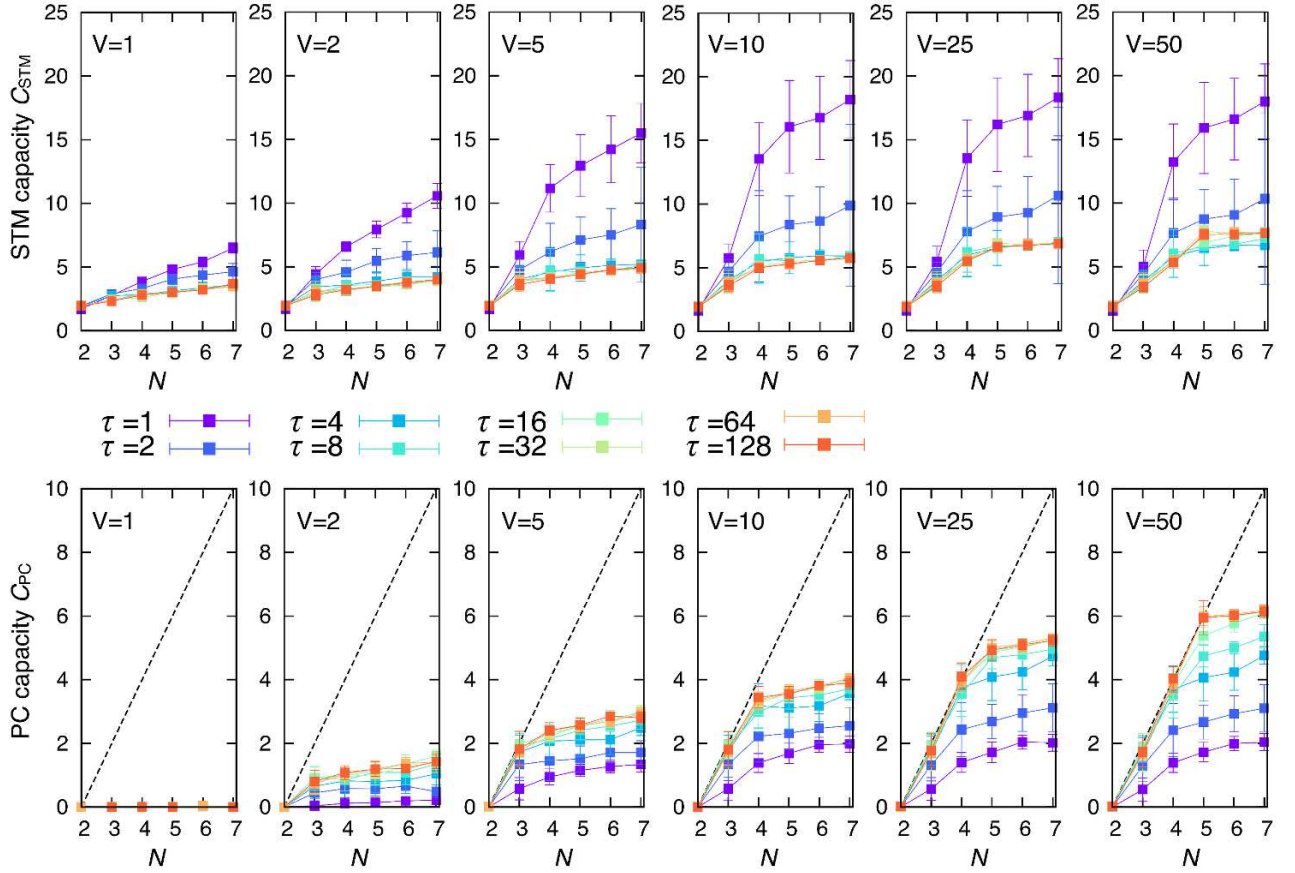


FIG. 10. Scaling of the STM and PC capacities against the number of the qubits. (Top) The STM capacity C_{STM} is plotted against the number of qubits N for each number of virtual nodes ($V = 1, 2, 5, 10, 25, 50$ from left to right). (Bottom) The PC capacity C_{PC} is plotted against the number of qubits N for each number of virtual nodes ($V = 1, 2, 5, 10, 25, 50$ from left to right). $C_{PC} = 2(N - 2)$ is shown by dotted lines.

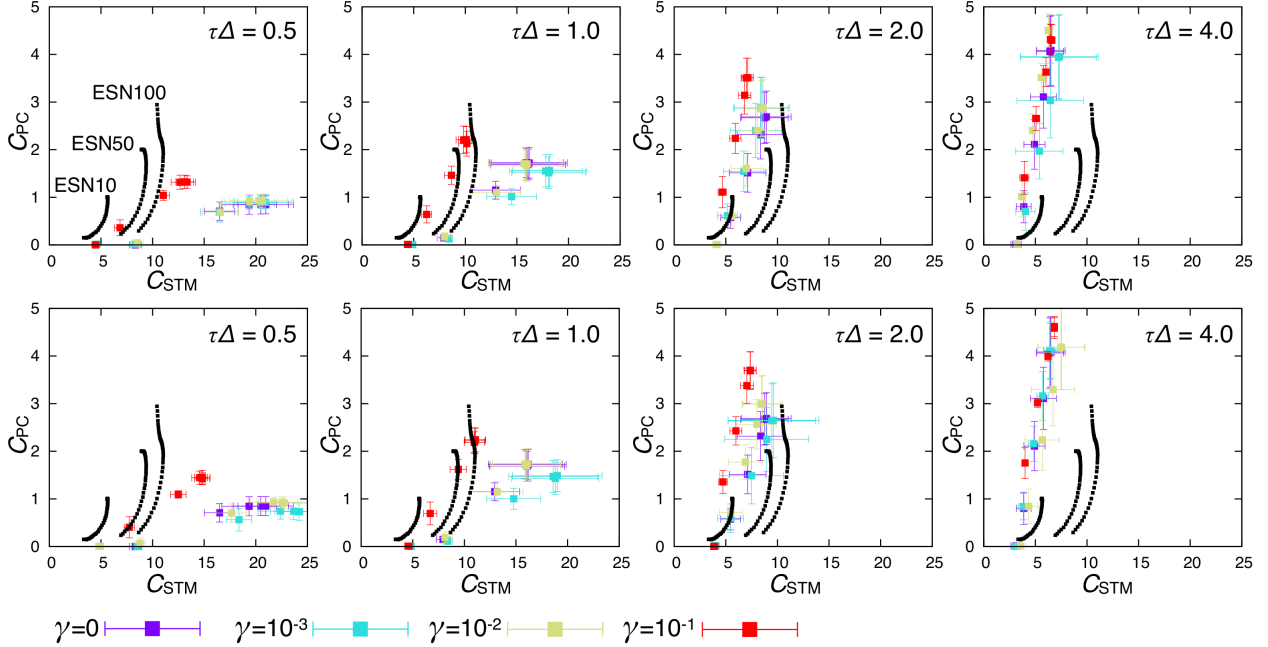


FIG. 11. **STM and PC capacities under decoherence investigated for the 5-qubit QRs.** The parameters are set as $\tau\Delta = 0.5, 1.0, 2.0, 4.0$ and $V = 1, 2, 5, 10, 25, 50$. (Top) Capacities (C_{STM}, C_{PC}) under dephasing in the z -axis are plotted for $\gamma = 10^{-2}, 10^{-3}, 10^{-4}$. (Bottom) Capacities (C_{STM}, C_{PC}) under dephasing in the x -axis are plotted for $\gamma = 10^{-2}, 10^{-3}, 10^{-4}$.

$e^{-2\gamma\delta t})/2$ for each timestep:

$$\mathcal{E}(\rho) = \frac{1 + e^{-2\gamma\delta t}}{2}\rho + \frac{1 - e^{-2\gamma\delta t}}{2}Z\rho Z. \quad (21)$$

This corresponds to a Markovian dephasing with a dephasing rate γ and destroys quantum coherence, i.e. off-diagonal elements in the density matrix. Apart from the dephasing in the z -direction, we also investigate the dephasing in x -direction, where the Pauli Z operator is replaced by X . In Fig. 11, the STM and PC capacities (C_{STM}, C_{PC}) are plotted for $\tau\Delta = 0.5, 1.0, 2.0$, and 4.0 (from left to right) with $V = 1, 2, 5, 10, 25$, and 50 and $\gamma = 10^{-1}, 10^{-2}$, and 10^{-3} . The results show that dephasing of the rates $10^{-2} - 10^{-3}$, which is within an experimentally feasible range, does not degrade computational capabilities. A subsequent increase in the dephasing rate causes the STM capacity to become smaller, especially for the case with a shorter time interval $\tau\Delta = 0.5$. On the other hand, the PC capacity is improved by increasing the dephasing rate. This behaviour can be understood as follows. The origin of quantum decoherence is the coupling with the untouchable environmental degree of freedom, which is referred to as a “reservoir” in the context of open quantum systems. Thus, decoherence implies an introduction of another dynamics with the degree of freedom in the “reservoir” computing framework. This leads to the decoherence-enhanced improvement of nonlinearity observed in Fig. 11, especially for a shorter τ with less rich dynamics. Of course, for a large decoherence limit, the system becomes classical, preventing us from fully exploiting the potential computational ca-

pability of the QRs. This appears in the degradation of the STM capacity. By attaching the environmental degree of freedom, the spatialised temporal information is more likely to leak outside the true nodes. Accordingly we cannot reconstruct a past input sequence from the signals of the true nodes. In other words, quantum coherence is important to retain information of the past input sequence within the addressable degree of freedom. In short, in the QRC approach, we do not need to distinguish between coherent dynamics and decoherence; we can exploit any dynamics on the quantum system as it is, which is monitored only from the addressable degree of freedom of the quantum system.

Next, we consider the statistical noise on the readout signal from the QRs. We investigate the STM and PC capacities by introducing Gaussian noise with zero mean and variance σ on the output signals as shown in Fig. 12. The introduction of statistical noise leads to a gradual degradation of the computational capacities. However, the degradation is not abrupt, which means that QRC would be able to function in a practical situation. Note that in the demonstration of the chaotic time series prediction, we introduce statistical noise to the readout signals with the aim of stabilising the learning process.

These tolerances against imperfections indicate that the proposed QRC framework soundly functions in realistic experimental setups as physical reservoir computing.

Quantum integrability and computational capability— Finally, we address the relation between integrability of

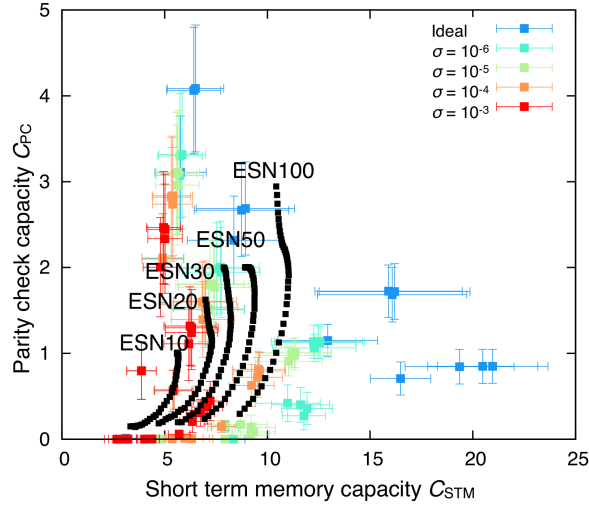


FIG. 12. **Effect of the statistical error on the readout signals investigated for the 5-qubit QRs.** The parameters are set as $\tau\Delta = 0.5, 1.0, 2.0, 4.0$ and $V = 1, 2, 5, 10, 25, 50$. The STM and PC capacities (C_{STM}, C_{PC}) are plotted for Gaussian noise with zero mean and variance $\sigma = 10^{-3}, 10^{-4}, 10^{-5}, 10^{-6}$.

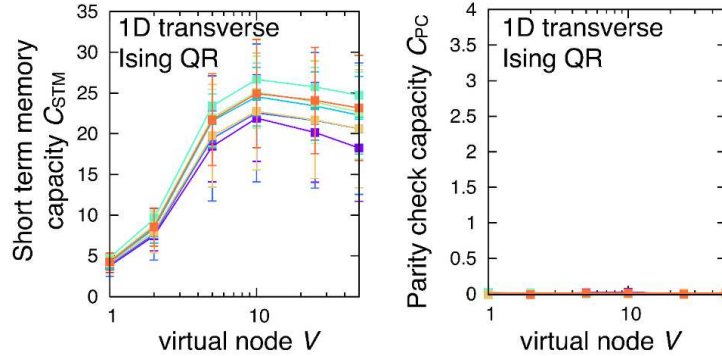


FIG. 13. **STM (left) and PC (right) capacities for the 1D transversal Ising model.**

the QR dynamics and its computational capability. In Fig. 5B of the main text, the real-time dynamics of QRs are shown for fully connected and 1D nearest-neighbour (1DNN) transversal Ising models. Specifically, in the 1DNN case, we can describe the dynamics as a closed formula for the $2N$ parameters (at most), by mapping the spin system into a free-fermionic system via the Jordan-Wigner transformation. Because the effective dimension of the state space is reduced from 2^{2N} to $2N$, the amplitudes of the oscillations are larger for the 1DNN case. From the real-time dynamics in Fig. 5B of the main text, one might expect a rich computational capability even for the integrable dynamics. Although this is true for the STM capacity, it does not hold for the PC capacity. As shown in Fig. 13, the STM capacity of the 1DNN

QRs is extremely high above 20. However, the PC capacity is substantially poor, which cannot improve even if the time intervals τ or the number of virtual nodes are changed. This is a natural consequence of the inability of the 1DNN model to fully employ exponentially large state spaces. In this way, the computational capacity of QRs, especially their nonlinear capacity, has a close connection with the nonintegrability of the underlying QR dynamics. This implies that the computational capacity as a QR provides a good metric of the integrability of quantum dynamics. A nonintegrable quantum system is identified as quantum chaos, which is specified by the Wigner-Dyson distribution of the energy eigenstate spacing. The operational metric of the integrability of quantum dynamics would be useful to build a modern operational understanding of quantum chaos by relating it to the emulatability of classical chaos.

-
- [1] Laje, R. & Buonomano, D.V. Robust timing and motor patterns by taming chaos in recurrent neural networks. *Nat. Neurosci.* **16**, 925-933 (2013).
- [2] Dambre, J., Verstraeten, D., Schrauwen, B. & Massar, S. Information processing capacity of dynamical systems. *Sci. Rep.* **2**, 514 (2012).
- [3] Atiya, A.F. & Parlos, A.G. New results on recurrent network training: Unifying the algorithms and accelerating convergence. *IEEE Trans. Neural Networks*, **11**, 697-709 (2000).
- [4] Verstraeten, D., Schrauwen, B., D’Haene, M. & Stroobandt, D. An experimental unification of reservoir computing methods. *Neural Netw.* **20**, 391-403 (2007).
- [5] Appeltant, L., Soriano, M.C., Van der Sande, G., Danckaert, J., Massar, S., Dambre, J., Schrauwen, B., Mirasso, C.R. & Fischer, I. Information processing using a single dynamical node as complex system. *Nat. Commun.* **2**, 468 (2011).
- [6] Hochreiter, S., Schmidhuber, J. Long short-term memory. *Neural Comput.* **9**, 1735-1780 (1997).
- [7] Hauser, H., Ijspeert, A.J., Fuchslin, R.M., Pfeifer, R. & Maass, W. Towards a theoretical foundation for morphological computation with compliant bodies. *Biol. Cybern.* **105**, 355-370 (2011).
- [8] Nakajima, K., Hauser, H., Kang, R., Guglielmino, E., Caldwell, D.G. & Pfeifer, R. Computing with a Muscular-Hydrostat System. In *Proceedings of 2013 IEEE International Conference on Robotics and Automation (ICRA)*, 1496-1503 (2013).
- [9] Nakajima, K., Hauser, H., Kang, R., Guglielmino, E., Caldwell, D.G. & Pfeifer, R. A soft body as a reservoir: case studies in a dynamic model of octopus-inspired soft robotic arm. *Front. Comput. Neurosci.* **7**, 1-19 (2013).
- [10] Nakajima, K., Hauser, H., Li, T. & Pfeifer, R. Information processing via physical soft body. *Sci. Rep.* **5**, 10487 (2015).
- [11] Nakajima, K., Li, T., Hauser, H. & Pfeifer, R. Exploiting short-term memory in soft body dynamics as a computational resource. *J. R. Soc. Interface* **11**, 20140437 (2014).
- [12] Jaeger, H. The “echo state” approach to analysing and training recurrent neural networks. GMD Report 148, German National Research Institute for Computer Science (2001).
- [13] Jaeger, H. & Haas, H. Harnessing nonlinearity: predicting chaotic systems and saving energy in wireless communication. *Science* **304**, 78-80 (2004).
- [14] Bertschinger, N. & Natschläger, T. Real-time computation at the edge of chaos in recurrent neural networks. *Neural Comput.* **16**, 1413-1436 (2004).
- [15] Jaeger, H. Tutorial on training recurrent neural networks, covering BPTT, RTRL, EKF and the “echo state network” approach. GMD Report 159, German National Research Center for Information Technology (2002).
- [16] Jaeger, H. Short term memory in echo state networks. GMD Report 152, German National Research Center for Information Technology (2001).